Mechanically Ultra-Robust Fluorescent Elastomer for Elaborating Auxetic Composite

Jiawei Li, Zhiran Zheng, Yaning Ma, Zhaoxing Dong, Min-Hui Li, Jun Hu

Mechanically Ultra-Robust Fluorescent Elastomer for Elaborating Auxetic Composite

*Jiawei Li, Zhiran Zheng, Yaning Ma, Zhaoxing Dong, Min-Hui Li, and Jun Hu**

J. Li, Z. Zheng, Y. Ma, Z. Dong, J. Hu
Beijing Advanced Innovation Center for Soft Matter Science and Engineering, Beijing University of Chemical Technology, North Third Ring Road 15, Chaoyang District, Beijing 100029, China
E-mail: jhu@mail.buct.edu.cn

J. Hu
State Key Laboratory of Polymer Physics and Chemistry, Changchun Institute of Applied Chemistry, Chinese Academy of Sciences, Renmin Street 5625, Chaoyang District, Changchun 130022, China

M.-H. Li
Chimie ParisTech, PSL University, CNRS, Institut de Recherche de Chimie Paris, 11 rue Pierre et Marie Curie, Paris 75005, France

Keywords: Fluorescent elastomer, high performance, hydrogen bonds, microphase separation, auxetic composite

Fluorescent elastomers are predominantly fabricated through doping fluorescent components or conjugating chromophores into polymer networks, which often involves detrimental effects on mechanical performance and also makes large-scale production difficult. Inspired by the heteroatom-rich microphase separation structures assisted by intensive hydrogen bonds in natural organisms, we report an ultra-robust fluorescent polyurethane elastomer, which features the remarkable fracture strength of 87.2 MPa with an elongation of 1797%, exceptional toughness of 678.4 MJ m^{-3} and intrinsic cyan fluorescence at 445 nm. Moreover, the reversible fluorescence variation with temperature could in situ reveal the microphase separation of the elastomer in real-time. By taking advantages of mechanical properties, intrinsic fluorescence and hydrogen bonds-promoted interfacial bonding ability, this fluorescent elastomer can be utilized as auxetic skeleton for the elaboration of an integrated auxetic composite. Compared with the auxetic skeleton alone, the integrated composite shows an improved mechanical

performance while maintaining auxetic deformation in a large strain below 185%, and its auxetic process can be visually detected under ultraviolet light by the fluorescence of the auxetic skeleton. The concept of introducing hydrogen-bonded heteroatom-rich microphase separation structures into polymer networks in this work provides a promising approach to developing fluorescent elastomers with exceptional mechanical properties.

1. Introduction

Fluorescent elastomers with extraordinary deformation and load-bearing capabilities are appealing to emerging applications in intelligent displays, flexible sensors, and metamaterials,[1-3] since the generation or variation of fluorescence signal in response to external stimuli can visually reveal the changes of stress and microstructure inside polymer networks.[4,5] At present, two strategies are widely used to construct fluorescent elastomers. The first strategy focuses on physically doping fluorescent components such as organic dyes, quantum dots, and rare-earth ions into a polymer matrix,[6-8] while the second one incorporates chemical conjugation of chromophores into elastomer networks.[9-11] Nevertheless, in the former strategy the poor interfacial compatibility between doping components and polymer matrix often inevitably leads to a decline in mechanical performance of elastomers. On the contrary, the specific reactive sites in elastomer backbone are required in the second strategy, and their complicated chemical synthesis also makes the large-scale production difficult. Additionally, the high mechanical strength of elastomers always features the migration-resistant molecular segments, which in turn compromises their elongation at break, causing the mutual exclusion between high strength and high toughness.[12,13] Therefore, the development of intrinsically fluorescent elastomers showing high strength and toughness presents great interest.

In nature, many organisms containing multiscale hydrogen-bonded (H-bonded) aggregates show exceptional mechanical properties and intrinsic fluorescence.[14-16] For instance, the remarkable comprehensive mechanical properties of spider silk arise from the incorporation of H-bonded β-sheet nanocrystals within an amorphous matrix. This delicate structure inspires researchers to make biomimetic elastomers by introducing H-bonded aggregates as hard phase into soft matrix for providing high strength, where the dynamic rupture and reformation effectively dissipate energy to improve the toughness.[17-21] Moreover, amyloids show intrinsic fluorescence originating in sufficient electron delocalization caused by hydrogen bonds (H-bonds) in cross-β-sheet structures containing hydroxyl, amide, and carboxyl groups rich in O and N heteroatoms.[22,23] This clusterization-triggered emission (CTE) characteristic is devoid of aromatic residues and extrinsic fluorescent labels, which reduces tedious synthetic procedures and eliminates any risk of deterioration in mechanical performance.[24] Thus, by

designing heteroatom-rich microphase separation structures assisted by intensive H-bonded hard phase and amorphous matrix, the simultaneous realization of high strength and high toughness of intrinsically fluorescent elastomers will be feasible.

Here, we developed a facile strategy of dynamic reinforcement for hard domains to fabricate a polyurethane elastomer PU-PIIA that possessed the combination of ultra-high strength, exceptional toughness, and intrinsic fluorescence (**Scheme 1**). Within the PU-PIIA, the incorporation of acylsemicarbazide (ASC) promoted the formation of intensive H-bonded hard domains, which embedded in soft domains to generate microphase separation structures showing extraordinary deformation and load-bearing capabilities. The resultant PU-PIIA exhibited a fracture strength of 87.2 MPa, true stress of 1.65 GPa at fracture, elongation at break of 1797%, and toughness of 678.4 MJ m^{-3}. Moreover, the effective dissipation of stress concentration in crack region endowed PU-PIIA with good crack tolerance, the fracture energy of which was up to 276 kJ m^{-2}. Benefiting from the through-space conjugation of electron-rich clusters induced by intensive H-bonds in hard domains, PU-PIIA exhibited intrinsic cyan fluorescence at 445 nm. The reversible fluorescence variation with temperature through the disintegration and recombination of electron-rich clusters could in situ reveal the microphase separation of PU-PIIA in real-time. Furthermore, by cutting PU-PIIA into an auxetic skeleton (PUAS) followed by embedding into a soft matrix, an integrated auxetic composite (PUAC) featuring a sophisticated skeleton-matrix architecture was elaborated. Compared with PUAS alone, the PUAC showed the improved mechanical properties with a fracture strength of 11.8 MPa, elongation at break of 470%, and toughness of 27.3 MJ m^{-3}, while maintaining good auxetic properties with negative Poisson's ratio (NPR) across a wide strain range from 0% to 185%. During this auxetic process, the intrinsic fluorescence originated from auxetic skeleton could visually detect the structure deformation of PUAC under UV light. This work addresses the challenges associated with the fabrication of fluorescent elastomers with exceptional mechanical properties, which provides a platform for constructing auxetic metamaterials with good mechanical performance and visualization of auxetic deformation.

2. Results and Discussion

2.1. Preparation and structure characterization of PU-PIIA elastomer

Scheme 1a illustrated the synthetic procedure of PU-PIIA. Initially, polytetramethylene ether glycol (PTMEG, M_n = 2 kDa) reacted with isophorone diisocyanate (IPDI) to give a prepolymer, and then continuously polymerized with IPDI and chain extender of adipic dihydrazide (ADH) to get polyurethane elastomer PU-PIIA. Due to the occurrence of the addition reaction between hydrazide and isocyanate groups with high fractions, abundant acylsemicarbazide (ASC)

moieties comprising urea and amide linkages were produced to implant between soft PTMEG segments. Consequently, a substantial multitude of donors and acceptors of H-bonds within ASC and urethane moieties promoted the aggregation of hard segments, engendering intensive H-bonded microdomains as the indispensable reinforcing constituents within microphase separation structures (Scheme 1b). The chemical structure of PU-PIIA was verified through the utilization of ^{1}H-Nuclear magnetic resonance (^{1}H-NMR) and Fourier transform infrared spectra (FTIR). The proton peaks at 2.92 and 4.04 ppm were attributed to methylene groups connected to urea and urethane, respectively, thereby affirming the accomplished conversion of isocyanate moieties with hydroxyl and hydrazide groups (Figure S1, Supporting Information). Moreover, the absence of characteristic peak corresponding to -NCO group at 2260-2280 cm^{-1} in FTIR indicated a complete reaction of isocyanate groups.[25] The absorption bands at 3284 and 1541 cm^{-1} were attributed to the stretching and bending vibration of N-H, while the peak at 1660 cm^{-1} was assigned to the stretching vibration of C=O, all of which were from the generated urethane and ACS units (Figure S2, Supporting Information).[26] Size exclusion chromatography (SEC) analysis provided additional insights into molecular weight (M_n) of PU-PIIA, which was determined to be 39 kDa, accompanied by a polydispersity index (PDI) of 1.3 (Figure S3, Supporting Information). All the aforementioned results collectively validated the complete polymerization in PU-PIIA.

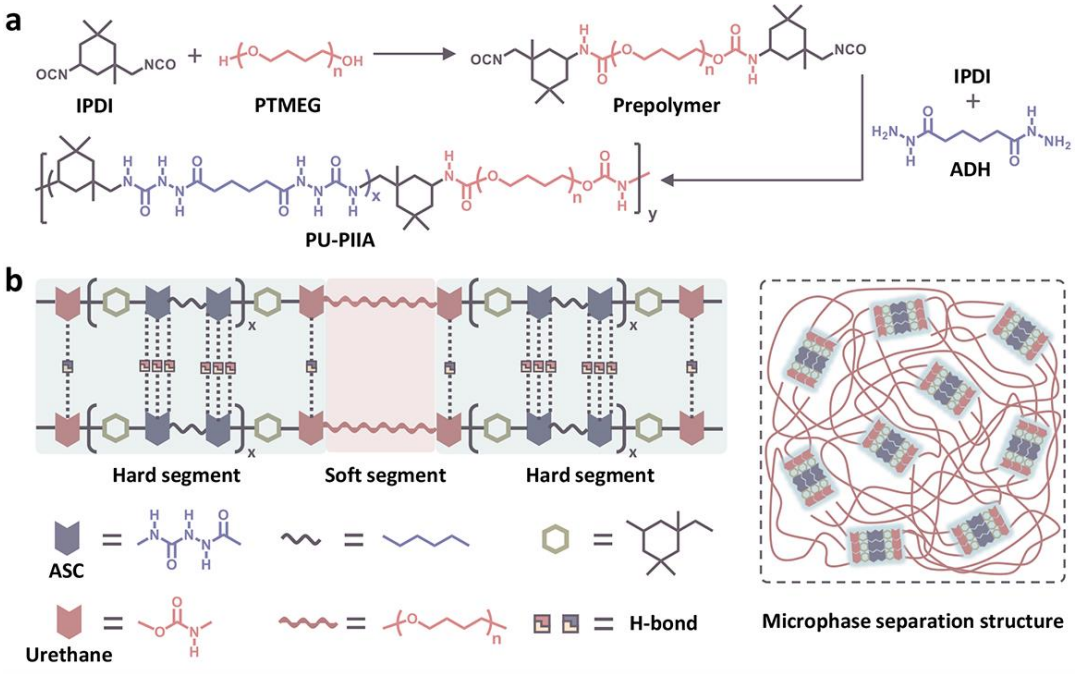

Scheme 1. Chemical structure and microstructure of PU-PIIA elastomer. a) Synthetic route and b) schematic structural diagram with microphase separation structures composed of the aggregated hard and soft segments.

The PU-PIIA elastomer was colorless with the transmittance over 85% across the visible light region (**Figure 1**a). X-ray diffractions (XRD) revealed the amorphous structure of PU-PIIA, which showed a broad bump at 2θ of 20° corresponding to an average lateral spacing of 0.44 nm between polymer backbones (Figure 1b). The amorphous structure was also verified by differential scanning calorimetry (DSC), where no crystalline exothermic peak was recorded within the temperature range spanning from -60 to 200°C (Figure S4, Supporting Information). 1D and 2D small-angle X-ray scattering (SAXS) clearly demonstrated the microphase separation structure of PU-PIIA (Figure 1c). The circular scattering ring indicated that hard domains were uniformly and densely dispersed in the soft phase dominated by PTEMG. The broad scattering peak at 0.58 nm^{-1} corresponded to the short-range ordered structure with a periodicity (L) of 10.8 nm. According to one-dimensional correlation function obtained from Fourier inversion of SAXS, the diameter of hard domains and their average distance were calculated to be 3.5 and 9.4 nm, respectively, along with the boundary of the transition zone around 1.0 nm (Figure 1d).[27] The modulus map of atomic force microscopy (AFM) further confirmed the microphase separation structure (Figure 1e). Eventuated by thermodynamic incompatibility between hard and soft segments, the bright area of high modulus corresponded to the H-bonded hard domains, while the dark continuous domains with low modulus represented the aggregation of PTMEG soft segments. By peak fitting and differentiation of C=O stretching vibration of PU-PIIA from 1600 to 1750 cm^{-1} in FTIR spectrum, the C=O band was deconvolved into six subpeaks assigning to free and H-bonded C=O in urethane, urea, and amide groups (Figure 1f).[28] The proportion of H-bonded C=O was up to 69% within PU-PIIA (Table S1, Supporting Information), conducive to the formation of intensive H-bonded aggregates in hard domains.

The thermal performance of PU-PIIA elastomer was evaluated through thermogravimetric analysis (TGA), dynamic mechanical analysis (DMA), and rheological measurements. The TGA curve revealed that the PU-PIIA exhibited an initial thermal decomposition temperature ($T_{5\%}$) of 294°C (Figure 1g). The presence of intensive H-bonded aggregates within hard domains significantly contributed to the high cohesion energy of polymer chains, leading to good thermal stability of PU-PIIA elastomer. Its thermal degradation process can be divided into two stages at 294-380°C and 380-490°C. The stage I mainly involved the thermal decomposition of urethane and ASC in hard segments, while the thermal decomposition in stage II was attributed to fatty chains in soft segments. DMA revealed that both storage and loss modulus of PU-PIIA decreased with the temperature increase, causing the ratio of storage modulus over loss modulus (tan δ) to change (Figure S5, Supporting Information). Two

relaxation peaks of tan δ at -76°C and 106°C corresponded to the glass transition temperature of soft PTMEG segments (T_{gs}) and H-bonded hard segments (T_{gh}), respectively (Figure 1h). Additionally, rheological measurement demonstrated that the solid-liquid transition of PU-PIIA elastomer occurred at 173°C (Figure 1i). In brief, the PU-PIIA elastomer exhibited heteroatom-rich microphase separation structures by incorporating ASC-dominant H-bonds-reinforced hard domains into amorphous soft domains, which was advantageous for its mechanical performance, as discussed in the following section.

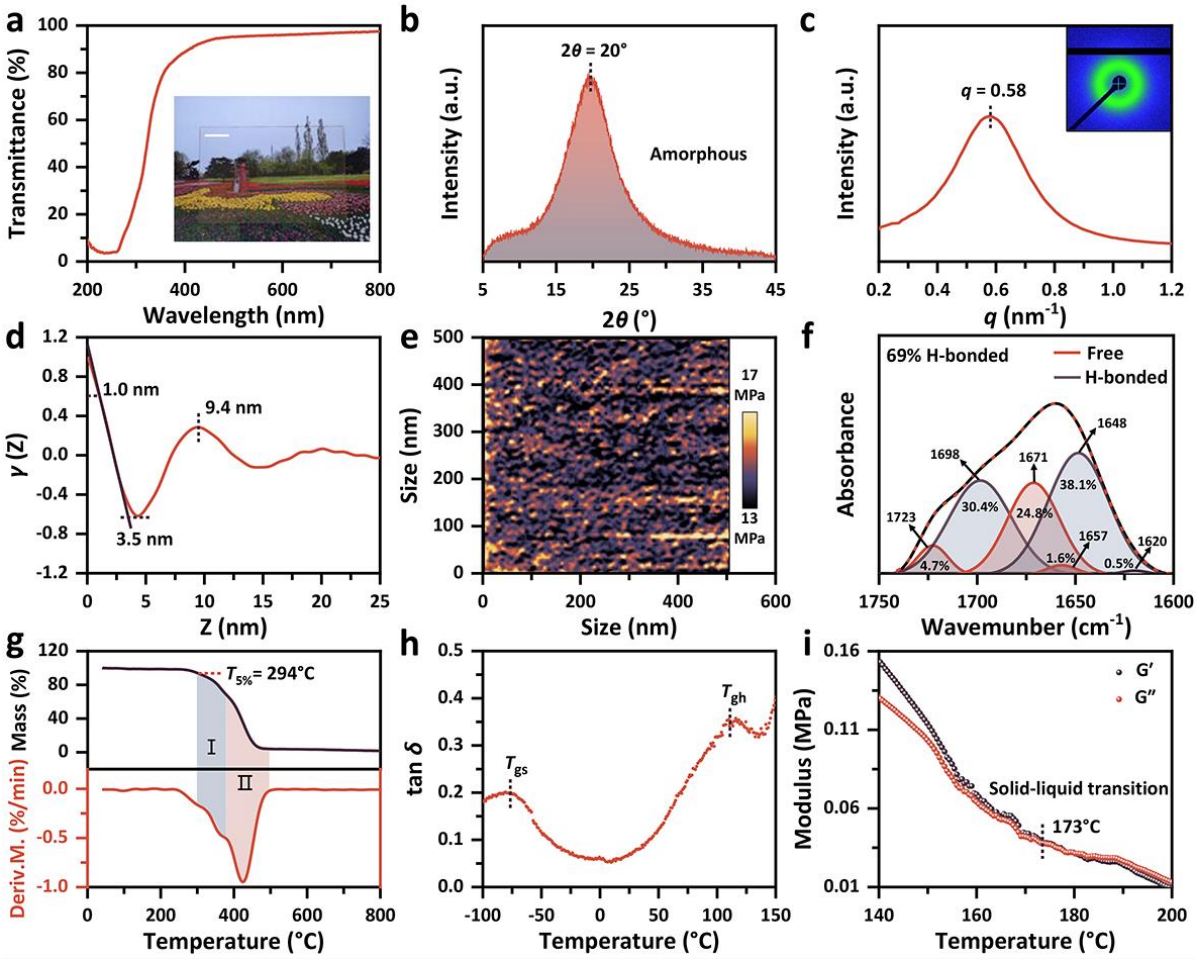

Figure 1. Structure characterization of PU-PIIA elastomer. a) Transmission spectrum across the wavelength range of 200 to 800 nm. Inset: photograph of PU-PIIA elastomer with a thickness of 0.8 mm. We hold the copyright for the background image, which was captured by our camera at the Beijing Botanical Garden. Scale bar was 2 cm. b) XRD pattern in 2θ range from 5 to 45° employing a scanning rate of 10° min^{-1}. c) 1D SAXS profile in q range from 0.2 to 1.2 nm^{-1}. Inset: 2D SAXS image. d) Correlation function obtained from SAXS results after Fourier inversion. e) AFM modulus map of a 500 × 500 nm^2 region. f) ATR-FTIR spectrum and its fitting curves in C=O stretching vibration region from 1600 to 1750 cm^{-1}. g) TGA and DTG curves within the temperature interval of 30°C to 800°C at a heating rate of 10°C min^{-1}. h) Tan

δ as a function of temperature over the range of -100 to 150°C. i) Temperature-dependent rheological behavior of PU-PIIA elastomer from 140 to 200°C with a frequency of 10 Hz under a strain of 1%.

2.2. Mechanical, resilience, and crack tolerance properties of PU-PIIA elastomer

The mechanical properties of PU-PIIA elastomer were assessed through a tensile test conducted at a tensile speed of 50 mm min^{-1}. PU-PIIA elastomer exhibited an extremely high fracture strength of 87.2 MPa along with an elongation at break of 1797%, and an exceptional toughness of 678.4 MJ m^{-3} (**Figure 2**a, Table S2, Supporting Information). Its true stress at break was even up to 1.65 GPa (Figure 2b), comparable to some of the most robust natural materials such as spider silks (0.8-1.5 GPa).[29] The extraordinary mechanical robustness was demonstrated by the fact that a thin strip of only 20 mg could successfully sustain a weight of 5.3 kg (265,000 times relative to its own weight) (inset in Figure 2b). To illustrate stress-induced microstructure evolution during stretching, 1D and 2D SAXS tests were performed. In the incipient stage of deformation, the circular scattering ring underwent a transformation into an ellipse with a principal axis. As the stretching continued up to 1500%, the signal gradually decayed along the longitudinal direction, revealing the re-arrangement of microdomains from isotropic to anisotropic (Figure 2c). Correspondingly, the scattering peak related to average interdomain distance between hard domains weakened in the initial stretch to 300%, accompanied by a shift of q from 0.58 to 0.40 nm^{-1}. In the subsequent deformation process, the peak gradually weakened with the location unchanged (Figure 2d). The fracture and recombination of H-bonds during the stretching process induced the reorientation, deformation, and dissociation of H-bonded domains, followed by slippage of polymer chains.[30] Consequently, the evolution of these microstructures synergistically dissipated more energy to diminish stress concentration, endowing PU-PIIA elastomer with high fracture strength and toughness. Compared with other reported fluorescent elastomers,[31-38] PU-PIIA elastomer showed outstanding advantages in fracture strength and toughness, and was even prominent among non-fluorescent elastomers especially in terms of toughness (Figure 2e, Table S3, Supporting Information).[26,39-50]

In order to accentuate the pivotal function of ASC moieties that encompassed intensive H-bonds as sacrificial bonds to enhance mechanical performance, another two control elastomers (PU-PIIT and PU-PIID) were synthesized, where terephthalic dihydrazide (THD) bearing a benzene ring and dodecanedioyl dihydrazide (DHD) comprising an alkyl chain were used as chain extenders instead of ADH (Scheme S1, Supporting Information). Compared with PU-PIIA, two control elastomers had similar transmittance but a much lower proportion of H-bonded C=O groups, which was 59% and 54% for PU-PIIT and PU-PIIT, respectively (Figure

S6 and S7, Table S1, Supporting Information). The decline in proportion of H-bonds was because the presence of rigid aromatic rings or flexible alkyl chains disturbed the formation of intensive H-bonded aggregates. As a result, PU-PIIA manifested better mechanical properties in comparison with PU-PIIT and PU-PIID (Figure S8, Table S2, Supporting Information).

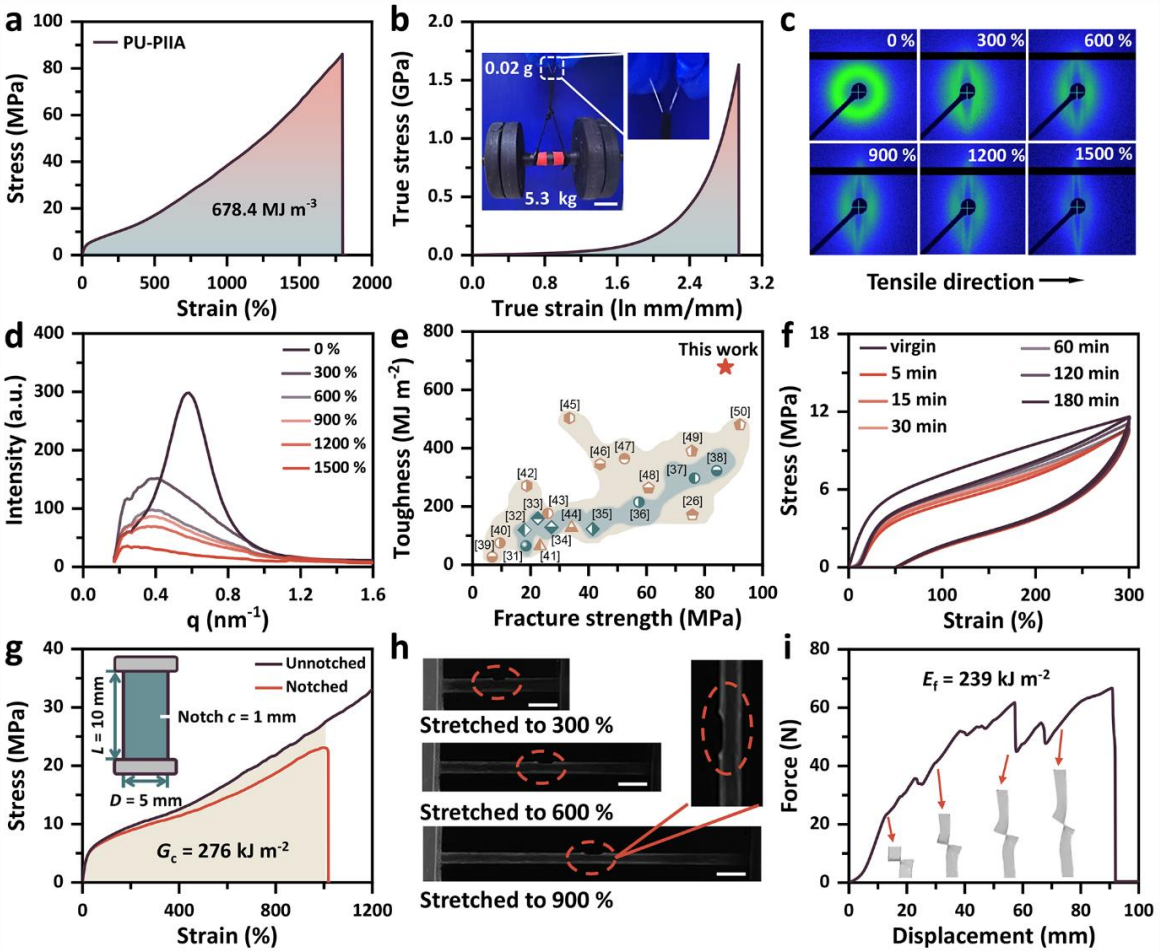

Figure 2. Mechanical, resilience, and crack tolerance properties of PU-PIIA elastomer. a) Typical engineering tensile stress-strain curve at a tensile speed of 50 mm min^{-1}, and b) the corresponding true stress-strain curves. Inset: photographs of elastomer strip (20 mg) with dimensions of 40 mm × 2 mm × 0.8 mm lifting a weight of 5.3 kg. Scale bar was 4 cm. c) 2D SAXS images under the stretching strain of 0%, 300%, 600%, 900%, 1200% and 1500%, and d) the corresponding 1D SAXS profiles in q range from 0.17 to 1.6 nm^{-1}. e) Comparison of PU-PIIA and other reported elastomers in fracture strength and toughness. Green and brown symbols represent fluorescent and non-fluorescent elastomers, respectively. f) Cyclic loading-unloading tensile curves at different waiting times under a tensile speed of 50 mm min^{-1}. g) Typical engineering tensile stress-strain curves of the unnotched and notched PU-PIIA with a size of 10 × 5 × 0.8 mm at a stretching rate of 3 mm min^{-1}. h) Photographs of the notched PU-PIIA elongated to different strains. Scale bar was 1 cm. i) Force-displacement curve of PU-PIIA measured by trouser tear tests. Inset: photographs of PU-PIIA in the trouser tear test.

Cyclic tensile experiments were performed to investigate the resilience of PU-PIIA elastomer. As illustrated in Figure S9 (Supporting Information), both hysteresis area and energy dissipation efficiency progressively expanded with the strain increased from 100% to 500%, revealing that PU-PIIA experienced elastic deformation accompanied by the gradient rupture of H-bonds in hard domains. Figure 2f presented the cyclic tensile curves of PU-PIIA after subjecting to a 300% strain and varying waiting times. The first loading-unloading curve exhibited a prominent hysteresis loop, indicating that the energy was consumed by the rupture of H-bonds and the intramural frictional resistance between molecular chains.[50] With the extension of waiting time, the cyclic curve gradually recovered and approached the initial state, with a residual strain eliminated to 6.2%. Evidently, this exceptional resilience of PU-PIIA elastomer was attributed to the dynamic dissociation and re-association of intensive H-bonds in hard domains.

In addition, notch stretching experiments were performed to evaluate the crack tolerance of PU-PIIA elastomer. In the presence of a notch of 1 mm, the fracture strength and elongation at break of PU-PIIA reached 23.1 MPa and 1015%, respectively, while exhibiting a remarkable fracture energy of 276 kJ m^{-2} (Figure 2g). During the stretching process, the crack extended along the stretching direction and did not propagate significantly until the fracture occurred (Figure 2h). The stress concentrated in the notched region was effectively alleviated by the dynamic fracture and recombination of H-bonds in hard domains, facilitating the motion of polymer chains to prevent crack propagation and improve reliability. This can be further evaluated by stretching a trouser specimen to break, where the tearing energy of PU-PIIA was up to 239 kJ m^{-2} (Figure 2i).

2.3. Intrinsic fluorescence property of PU-PIIA elastomer

As depicted in **Figure 3**a, PU-PIIA elastomer manifested intrinsic cyan fluorescence with an emission peak of 445 nm. With the formation of electron-rich clusters induced by intensive H-bonds within PU-PIIA networks, the occurrence of effective electronic interactions promotes the delocalization of electrons in space, leading to the extended spatial conjugation within the clusters that which restricted the intramolecular motions and facilitated the radiation transition under UV irradiation.[51,52] This clusterization-triggered emission (CTE) did not involve the physical doping or chemical modification of fluorescence components, avoiding the laborious preparation procedures and detrimental effects of fluorescent additives on mechanical properties. In general, invisible fluorescent patterns applied to anti-counterfeiting protective coatings can be seen under UV light but not recognized by the naked eyes. As shown in Figure 3b, PU-PIIA was physically cut into letter shapes of “B”, “U”, “C”, and “T”, and then placed

on the surface of polydimethylsiloxane (PDMS) film. Fluorescent patterns were revealed clearly when exposed to UV light at 365 nm. After clamping PU-PIIA with a rabbit pattern between two layers of PDMS films, the pattern was invisible, while emerged immediately under irradiation of UV light.

It was noteworthy that the intrinsic fluorescence of PU-PIIA elastomer was sensitive to mechanical force and temperature. As the tensile deformation escalated from 0% to 800%, the progressive breaking of H-bonds precipitated the disintegration of electron-rich clusters, consequently attenuating the fluorescence intensity (Figure 3c). Accordingly, the corresponding gray value of fluorescent images exhibited a pronounced decline, facilitating the assessment of fluorescence sensitivity toward mechanical forces. Furthermore, the cyan fluorescence of PU-PIIA gradually weakened and eventually vanished with elevating temperature from 40 to 160°C, while recovered again upon cooling (Figure 3d). During this reversible process, the fluorescence intensity at 445 nm experienced a reduction of approximately 60% at 160°C, while returned to its original state when the temperature dropped back to 40°C (Figure 3e). This was closely related to the dynamic dissociation and recombination of H-bonds. The dissociation of hydrogen bonds as the elevated temperature attenuated the aggregation of electron-rich clusters, resulting in a decrease in fluorescence intensity. On the contrary, upon cooling the progressive re-association of hydrogen bonds promoted the aggregation of electron-rich clusters again, accompanied by the recovery of fluorescence intensity. This process was further validated by temperature-dependent FTIR spectra. The peak fitting and differentiation methods were employed for the absorption band in 1750-1500 cm^{-1} to calculate the proportion of free and H-bonded C=O at different temperatures (Figure S10, Supporting Information). As shown in Figure 3f and detailed in Table S4 (Supporting Information), the absorption bands of free C=O assigned to urethane, urea, and amide groups at 1723, 1671, and 1657 cm^{-1} exhibited a gradual augmentation with increasing temperature, whereas the peaks corresponding to H-bonded C=O from urethane at 1698 cm^{-1}, urea at 1648 cm^{-1}, and amide at 1620 cm^{-1} underwent a decline in intensity. In addition, the weakening peak at 1546 cm^{-1} was assigned to the bending vibration of H-bonded N-H groups, while the intensifying band at 1525 cm^{-1} was attributed to free N-H groups. All these results indicated that the increase of temperature activated the rupture of H-bonds for the destruction of electron-rich clusters, resulting in a defined relationship between the H-bonds proportion and intrinsic fluorescence intensity of PU-PIIA (Figure 3g).[53]

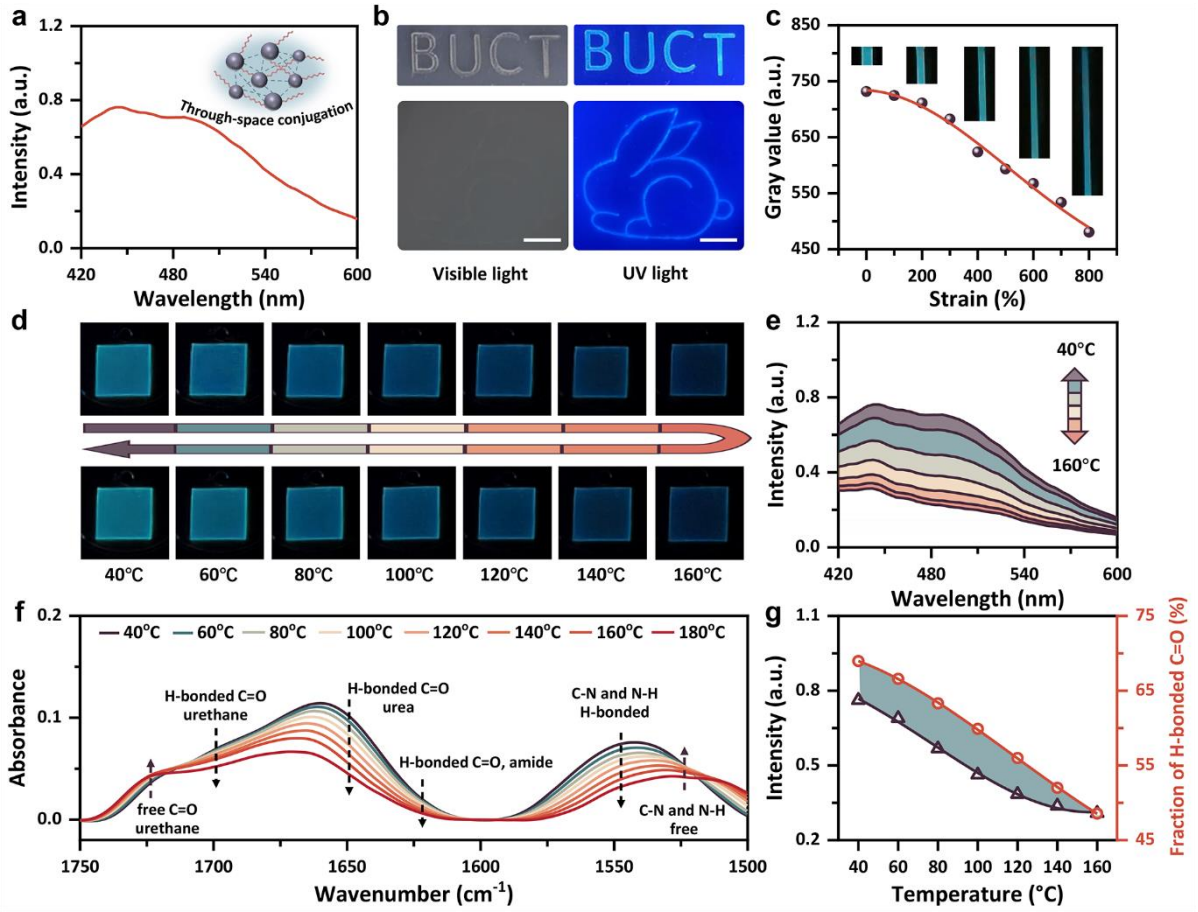

Figure 3. Intrinsic fluorescence property of PU-PIIA elastomer. a) Fluorescence spectrum in the wavelength range from 420 to 600 nm. Inset: schematic diagram of the through-space conjugation of electron-rich clusters induced by H-bonds. Purple spheres, red wavy lines, and blue dashed lines represented hard segments, soft segments, and H-bonds, respectively. b) Photographs of the patterned-PU-PIIA under visible light and 365 nm UV light. The patterned elastomer samples were prepared by CO_2 laser cutting. Scale bar was 1 cm. c) Mean gray value of fluorescent images of PU-PIIA as a function of strain. Inset: fluorescence images. d) Fluorescent photographs at temperature increasing from 40 to 160°C and decreasing from 160 to 40°C, and e) the corresponding fluorescence spectra. f) Temperature-dependent FTIR spectra upon heating from 40°C to 180°C. g) Plots of the proportion of H-bonded C=O and fluorescence intensity at 445 nm as a function of temperature.

2.4. Elaboration, mechanical, and auxetic properties of PUAC

Auxetic materials are able to expand/contract transversely when subjected to longitudinal tensile/compression, showing distinctive deformation features with negative Poisson's ratio (NPR).[54] To achieve auxeticity, the introduction of cellular structures with geometrical configurations into polymer materials is frequently necessitated.[55,56] Nevertheless, the mechanical properties of these auxetic materials such as fracture strength and elongation at

break are significantly compromised during the pore-making processes. Numerous natural organisms are hybrid composites composed of heterogeneous materials with skeleton-matrix structures, exhibiting attractive mechanical properties and functionality inaccessible by their separate components alone.[57,58] Drawing inspiration from the skeleton-matrix structures found in natural organisms, the construction of the integrated structure comprising of auxetic skeleton and soft matrix would be an effective strategy to improve the mechanical properties of auxetic materials. Within this integrated composite, the auxetic skeleton necessitates not only high mechanical properties for bearing the load but also the ability to establish a steady interfacial bond with the matrix. Obviously, PU-PIIA elastomer, driven by the intensive hydrogen bonds in the heteroatom-rich microphase separation structures, meets these requirements and is a suitable candidate for skeleton materials. Furthermore, its intrinsic fluorescence can also facilitate the deformation visualization of the integrated composite. The corrugated re-entrant structure with curved constituent elements has been specifically designed to prepare auxetic skeleton due to the good stress dissipation and the adjustable structure parameters.[59-61] As illustrated in **Figure 4**a, PU-PIIA elastomer underwent an initial laser cutting process to fashion an auxetic skeleton (PUAS) with a corrugated re-entrant structure, the geometric parameters of which were summarized in Figure S11 (Supporting Information). Meanwhile, a flexible PU-PIE elastomer was designed as the matrix by substituting ADH with ethylene glycol (EG) as chain extender (Scheme S2, Supporting Information), which was much softer than PU-PIIA (Figure S12 and Table S2, Supporting Information). After infusing the prepolymer of PU-PIE into PUAS in shape-complementary manner followed by complete polymerization at 80°C, the integrated auxetic composite (PUAC) with skeleton-matrix structure was successfully obtained. Within PUAC, the hard skeleton of PUAS effectively assumed the burden of applied loads to impart the strength, and the soft PU-PIE transferred stress concentrated on skeleton under a biaxial loading status to promote favorable stress distribution and energy dissipation.

The resultant PUAC was a void-free solid, and its corrugated re-entrant structure was conspicuously displayed under UV light (Figure 4b). Due to the infiltration of PU-PIE into the skeleton and the H-bonds between skeleton and matrix, no sharp soft-to-hard interface was observed in PUAC. Tensile tests showed that PUAC had a fracture strength of 11.8 MPa, elongation at break of 470%, and toughness of 27.3 MJ m^{-3}, better than that of PUAS alone (Figure 4c and Figure S13, Supporting Information), which demonstrated that the introduction of soft matrix significantly bolstered the mechanical properties of PUAS. Finite element analysis (FEA) can effectively evaluate the structural deformation and stress distribution, and the mesh size options of PUAS and PUAC in FEA were shown in Figure S14 (Supporting

Information). High strain levels were observed at the center of axial ribs of PUAS due to the large axial deformation, and the matrix in PUAC also underwent extension deformation under the traction of auxetic skeleton (ESTRN Contour Plots, Figure 4d). On the contrary, stress concentration points corresponding to high strain levels were discernible in the stress field distribution of PUAS, while PUAC showed that the stress distribution on skeleton was relatively uniform without noticeable stress concentration, promoted by the stress transfer of PU-PIE matrix (Mises Stress Contour Plots, Figure 4e). Apparently, the PU-PIE matrix would dissipate stress to improve the strength and toughness of PUAC when subjected to external stress. During the tensile process, the lateral and axial strains of PUAC and PUAS were recorded. Similar to PUAS, the Poisson's ratio of PUAC remained negative in a wide deformation range of 0-185% (Figure 4f and S15, Supporting Information). Figure 4g intuitively showed the optical photographs and Poisson's ratio (v) of PUAC under visible light and UV light at 365 nm at different strain ratios. The values of v were recorded as -0.33, -0.22, -0.12, and -0.08 at a strain of 15%, 30%, 45%, and 60% in PUAC. The infused PU-PIE exhibited negligible restrictions on the bending and rotation of the skeleton in PUAC subjected to axial loading, thereby facilitating the retention of desirable auxetic properties in PUAC. In addition, the intrinsic fluorescence of skeleton visually manifested the auxetic deformation of PUAC when exposed to UV light in contrast to the limited visibility observed under visible light. Obviously, by elaborating the skeleton-matrix structure from PUAS and PU-PIE, the integrated composite PUAC exhibited good mechanical properties, large auxetic deformation, and intrinsic fluorescence. These advantages endowed PUAC with great potentials in in fields of tissue engineering, flexible sensors and wearable devices,[62-63] which will be explored in our future work.

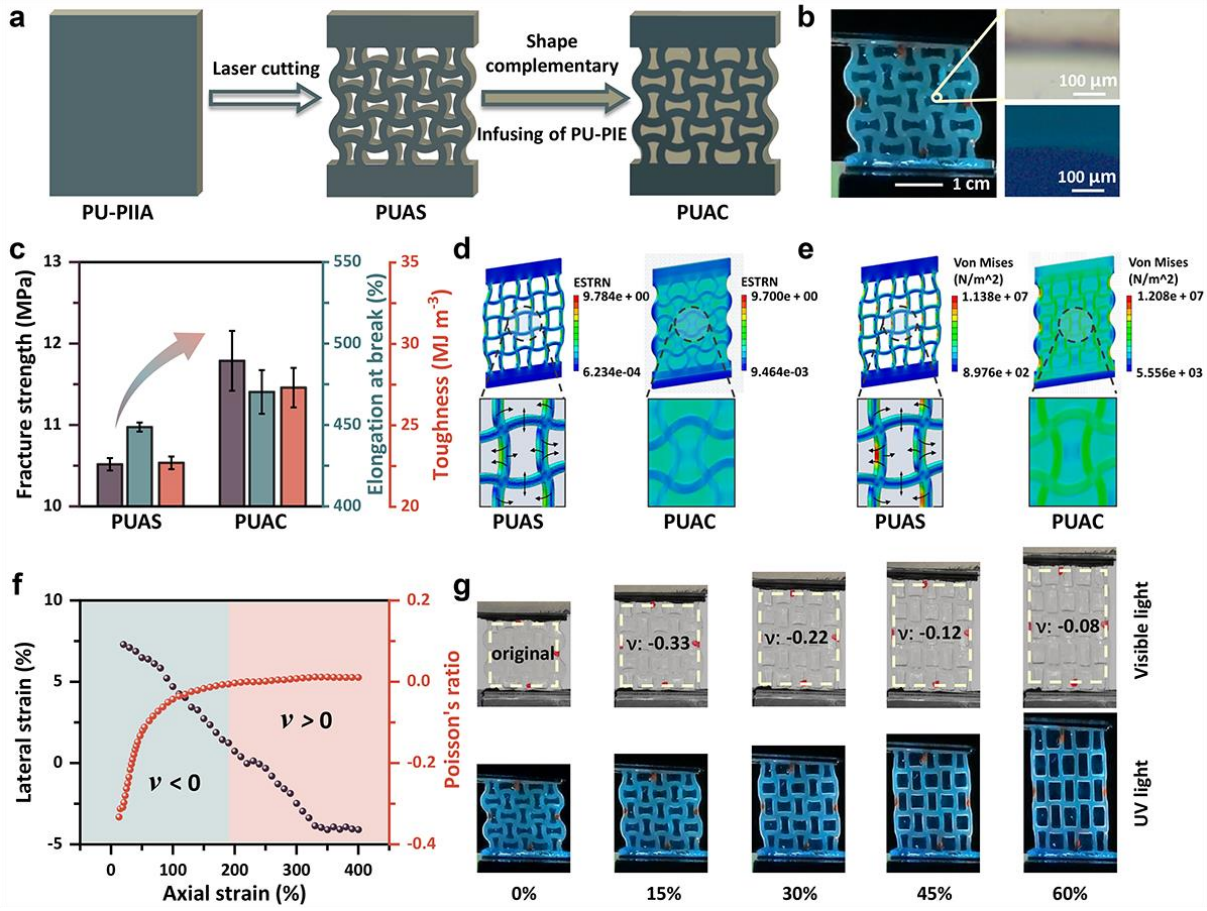

Figure 4. Integrated skeleton-matrix auxetic composite (PUAC) featuring good mechanical, auxetic, and fluorescent properties. a) Schematic illustration for the elaboration of PUAC using PUAS as hard skeleton and PU-PIE as soft matrix. b) Photographs of PUAC under UV light and its interfaces between skeleton and matrix. c) Values of fracture strength, elongation at break, and toughness of PUAS and PUAC. d) ESTRN and e) Von Mises of PUAS and PUAC under the tensile mode in FEA. A color bar from crimson to azure represented the simulated values transitioning from high to low, thereby qualitatively manifesting the distribution of stress and strain. f) Lateral strain and Poisson's ratio of PUAC as a function of axial strain during the tensile process. g) Experimental screenshots of PUAC under visible light and UV light at 365 nm from its initial state to an elongation of 60%. The rectangle dashed lines delineated the region of shape morphing.

3. Conclusion

In summary, we have synthesized a transparent fluorescent polyurethane elastomer (PU-PIIA) using a facile dynamic reinforced strategy. Due to the existence of intensive H-bonds in hard domains within the microphase separation structures, PU-PIIA elastomer simultaneously possessed the ultra-high strength, exceptional toughness, and intrinsic fluorescence. Moreover, the reversible fluorescence variation with disintegration and recombination of electron-rich

clusters could reveal the microphase separation of PU-PIIA in real-time. By taking advantages of ultra-high mechanical strength and intrinsic fluorescence, PU-PIIA was used to elaborate an integrated auxetic composite (PUAC) with skeleton-matrix structure, which showed good mechanical and auxetic properties with negative Poisson's ratio across a wide range of deformations. This work addresses the challenges associated with the fabrication of elastomers with high mechanical properties and intrinsic fluorescence, paving a promising avenue for advanced metamaterials in engineering applications. The heterogeneous material structure also allows the integrated auxetic composite to serve as a flexible stretchable matrix to integrate diverse functionalities. The unique topological structures and mechanical properties of auxetic composite are expected to further promote the development of functional elastomers in fields such as soft robots and intelligent sensors.

Statistical Analysis

All data were obtained from at least three independent samples and expressed as the mean ± standard deviation (n = 3 for polymer characterization; n = 5 for mechanical studies).

Supporting Information

Supporting Information is available from the Wiley Online Library or from the author.

Acknowledgements

This work is supported by Beijing Natural Science Foundation (L233016) and the Open Research Fund of State Key Laboratory of Polymer Physics and Chemistry, Changchun Institute of Applied Chemistry, Chinese Academy of Sciences.

Conflict of Interest

The authors declare no conflict of interest.

Data Availability Statement

Research data are not shared.

Received: ((will be filled in by the editorial staff))
Revised: ((will be filled in by the editorial staff))
Published online: ((will be filled in by the editorial staff))

References

[1] W. Yao, Q. Tian, J. Shi, C. Luo, W. Wu, *Adv. Funct. Mater.* **2021**, 31, 2100211.

[2] S. Zheng, T. Zhu, Y. Wang, T. Yang, W. Z. Yuan, *Angew. Chem. Int. Ed.* **2020**, 59, 10018.

[3] T. Hu, T. Pan, D. Guo, Y. Xiao, F. Li, M. Gao, Z. Huang, J. Zhu, T. Cheng, Y. Lin, *ACS Nano* **2023**, 17, 22035-22045.

[4] Y. Chen, G. Sanoja, C. Creton, *Chem. Sci.* **2021**, 12, 11098.

[5] J. Kim, J. Steck, *Matter* **2022**, 5, 2545.

[6] S. Furukawa, H. Shono, T. Mutai, K. Araki, *ACS Appl. Mater. Interfaces* **2014**, 6, 16065.

[7] J. Tan, R. Zou, J. Zhang, W. Li, L. Zhang, D. Yue, *Nanoscale* **2016**, 8, 4742.

[8] W. Yao, X. Chen, Q. Tian, C. Luo, X. Zhang, H. Peng, W. Wu, *Chem. Eng. J.* **2020**, 384, 123375.

[9] S. Zhao, J. Sun, Z. Qin, Y. Li, H. Yu, G. Wang, X. Gu, K. Pan, *Small* **2022**, 18, 2201117.

[10] K. Seshimo, H. Sakai, T. Watabe, D. Aoki, H. Sugita, K. Mikami, Y. Mao, A. Ishigami, S. Nishitsuji, T. Kurose, H. Ito, H. Otsuka, *Angew. Chem. Int. Ed.* **2021**, 60, 8406.

[11] S. Kumar Raut, S. Sarkar, P. Mondal, A. Meldrum, N. K. Singha, *Chem. Eng. J.* **2023**, 453, 139641.

[12] M. Vatankhah-Varnosfaderani, W. F. M. Daniel, M. H. Everhart, A. A. Pandya, H. Liang, K. Matyjaszewski, A. V. Dobrynin, S. S. Sheiko, *Nature* **2017**, 549, 497.

[13] R. O. Ritchie, *Nat. Mater.* **2011**, 10, 817.

[14] Q. Wang, P. McArdle, S. L. Wang, R. L. Wilmington, Z. Xing, A. Greenwood, M. L. Cotten, M. M. Qazilbash, H. C. Schniepp, *Nature Communications* **2022**, 13, 4329.

[15] T. P. Knowles, M. J. Buehler, *Nat. Nanotechnol.* **2011**, 6, 469.

[16] L. Del Mercato, P. Pompa, G. Maruccio, A. Della Torre, S. Sabella, A. Tamburro, R. Cingolani, R. Rinaldi, *Proc. Natl. Acad. Sci. U. S. A.* **2007**, 104, 18019.

[17] S. Keten, Z. Xu, B. Ihle, M. J. Buehler, *Nat. Mater.* **2010**, 9, 359.

[18] Z. Zhang, J. Luo, S. Zhao, S. Ge, J.-M. Y. Carrillo, J. K. Keum, C. Do, S. Cheng, Y. Wang, A. P. Sokolov, P.-F. Cao, *Matter* **2022**, 5, 237.

[19] N. J.-A. Chan, D. Gu, S. Tan, Q. Fu, T. G. Pattison, A. J. O'Connor, G. G. Qiao, *Nat. Commun.* **2020**, 11, 1630.

[20] Y. Eom, S. M. Kim, M. Lee, H. Jeon, J. Park, E. S. Lee, S. Y. Hwang, J. Park, D. X. Oh, *Nat. Commun.* **2021**, 12, 621.

[21] P. Song, H. Wang, *Adv. Mater.* **2020**, 32, 1901244.

[22] L. Hecker, W. Wang, I. Mela, S. Fathi, C. Poudel, G. Soavi, Y. Y. S. Huang, C. F. Kaminski, *Nano Lett* **2021**, 21, 938.

[23] O. Makin, E. Atkins, P. Sikorski, J. Johansson, L. Serpell, *Proc. Natl. Acad. Sci. U. S. A.* **2005**, 102, 315.

[24] H. Zhang, Z. Zhao, P. R. McGonigal, R. Ye, S. Liu, J. W. Y. Lam, R. T. K. Kwok, W. Z. Yuan, J. Xie, A. L. Rogach, B. Z. Tang, *Mater. Today* **2020**, 32, 275.

[25] C. Jiang, L. Zhang, Q. Yang, S. Huang, H. Shi, Q. Long, B. Qian, Z. Liu, Q. Guan, M. Liu, R. Yang, Q. Zhao, Z. You, X. Ye, *Nat. Commun.* **2021**, 12, 4395.

[26] Y. Huang, H. Wu, W. Li, Z. Yuan, Q. Wu, R. Li, J. Wu, *J. Mater. Chem. A* **2022**, 10, 24290.

[27] X. Guo, J. Liang, Z. Wang, J. Qin, Q. Zhang, S. Zhu, K. Zhang, H. Zhu, Adv. Mater. 2023, 35, 2210092.

[28] J. Wu, L. H. Cai, D. A. Weitz, *Adv. Mater.* **2017**, 29, 1702616.

[29] F. G. Omenetto, D. L. Kaplan, *Science* **2010**, 329, 528.

[30] Y. Zhuo, Z. Xia, Y. Qi, T. Sumigawa, J. Wu, P. Sestak, Y. Lu, V. Hakonsen, T. Li, F. Wang, W. Chen, S. Xiao, R. Long, T. Kitamura, L. Li, J. He, Z. Zhang, *Adv. Mater.* **2021**, 33, 2008523.

[31] L. Song, T. Zhu, L. Yuan, J. Zhou, Y. Zhang, Z. Wang, C. Tang, *Nat. Commun.* **2019**, 10, 1315.

[32] X. Qiu, Q. Cui, Q. Guo, T. Zhou, X. Zhang, M. Tian, *Small* **2022**, 18, 2107164.

[33] H. Chen, Z. Sun, H. Lin, C. He, D. Mao, *Adv. Funct. Mater.* **2022**, 32, 2204263.

[34] X. Wu, H. Li, P. Chen, J. Zhang, M. Li, S. Zhao, Z. Wang, Z. Wang, *J. Mater. Chem. A* **2023**, 11, 6286.

[35] Z. Yuan, J. Yan, F. Gao, J. Cheng, J. Zhang, *J. Mater. Chem. C* **2023**, 11, 8971.

[36] X. Chen, Q. Zhong, C. Cui, L. Ma, S. Liu, Q. Zhang, Y. Wu, L. An, Y. Cheng, S. Ye, X. Chen, Z. Dong, Q. Chen, Y. Zhang, *ACS Appl. Mater. Interfaces* **2020**, 12, 30847.

[37] X. Wang, J. Xu, Y. Zhang, T. Wang, Q. Wang, S. Li, Z. Yang, X. Zhang, *Nat. Commun.* **2023**, 14, 4712.

[38] X. Wang, J. Xu, X. Zhang, Z. Yang, Y. Zhang, T. Wang, Q. Wang, *Adv. Mater.* **2022**, 34, 2205763.

[39] S. M. Kim, H. Jeon, S. H. Shin, S. A. Park, J. Jegal, S. Y. Hwang, D. X. Oh, J. Park, *Adv. Mater.* **2018**, 30, 1705145.

[40] M. W. M. Tan, G. Thangavel, P. S. Lee, *Adv. Funct. Mater.* **2021**, 31, 2103097.

[41] Y. Xiao, P. Liu, W.-J. Wang, B.-G. Li, *Macromolecules* **2021**, 54, 10381.

[42] Q. Qu, J. He, Y. Da, M. Zhu, Y. Liu, X. Li, X. Tian, H. Wang, *Macromolecules* **2021**, 54, 8243.

[43] W. B. Ying, G. Wang, Z. Kong, C. K. Yao, Y. Wang, H. Hu, F. Li, C. Chen, Y. Tian, J. Zhang, R. Zhang, J. Zhu, *Adv. Funct. Mater.* **2021**, 31, 2009869.

[44] L. Xia, H. Tu, W. Zeng, X. Yang, M. Zhou, L. Li, X. Guo, *J.Mater. Chem. A* **2022**, 10, 4344.

[45] D. Wang, Z. Wang, S. Ren, J. Xu, C. Wang, P. Hu, J. Fu, *Mater. Horiz.* **2021**, 8, 2238.

[46] Y. Song, Y. Liu, T. Qi, G. L. Li, *Angew. Chem. Int. Ed.* **2018**, 57, 13838.

[47] X. Wang, S. Zhan, Z. Lu, J. Li, X. Yang, Y. Qiao, Y. Men, J. Sun, *Adv. Mater.* **2020**, 32, 2005759.

[48] W. Liu, C. Fang, S. Wang, J. Huang, X. Qiu, *Macromolecules* **2019**, 52, 6474.

[49] Z. Li, Y. L. Zhu, W. Niu, X. Yang, Z. Jiang, Z. Y. Lu, X. Liu, J. Sun, *Adv. Mater.* **2021**, 33, 2101498.

[50] R. Guo, Q. Zhang, Y. Wu, H. Chen, Y. Liu, J. Wang, X. Duan, Q. Chen, Z. Ge, Y. Zhang, *Adv. Mater.* **2023**, 35, 2212130.

[51] Q. Zhou, B. Cao, C. Zhu, S. Xu, Y. Gong, W. Z. Yuan, Y. Zhang, *Small* **2016**, 12, 6586.

[52] R. B. Restani, P. I. Morgado, M. P. Ribeiro, I. J. Correia, A. Aguiar-Ricardo, V. D. Bonifacio, *Angew. Chem. Int. Ed.* **2012**, 51, 5162.

[53] Y. Zhang, Y. Li, H. Wang, Z. Zhang, Y. Feng, Q. Tian, N. Li, J. Mei, J. Su, H. Tian, *ACS Appl. Mater. Interfaces* **2019**, 11, 39351.

[54] A. Papadopoulou, J. Laucks, S. Tibbits, *Nat. Rev. Mater.* **2017**, 2,17078.

[55] J. I. Lipton, R. MacCurdy, Z. Manchester, L. Chin, D. Cellucci, D. Rus, *Science* **2018**, 360, 632.

[56] K. K. Dudek, J. A. I. Martinez, G. Ulliac, L. Hirsinger, L. Wang, V. Laude, M. Kadic, *Adv. Mater.* **2023**, 35, 2210993.

[57] M. J. Allen, H. M. Lien, N. Prine, C. Burns, A. K. Rylski, X. Gu, L. M. Cox, F. Mangolini, B. D. Freeman, Z. A. Page, *Adv. Mater.* **2023**, 35, 2210208.

[58] F. Barthelat, Z. Yin, M. J. Buehler, *Nat. Rev. Mater.* **2016**, 1, 16007.

[59] A. Álvarez-Trejo, E. Cuan-Urquizo, D. Bhate, A. Roman-Flores, *Mater. Des.* **2023**, 233, 112190.

[60] Z. Zheng, J. Li, K. Wei, N. Tang, M.-H. Li, J. Hu, *Adv. Mater.* **2023**, 35, 2304631.

[61] M. Gómez-Castañeda, E. Cuan-Urquizo, A. L. Giraldo-Betancur, C. Félix-Martínez, A. Gómez-Ortega, J. M. Alvarado-Orozco, *Prog. Addit. Manuf.* **2024**, 9, 315.

[62] Y. Li, P. Chen, Z. Wu, C. Shi, P. Chen, Y. Xu, X. Chen, M. Chen, Y. Li, C. Yan, Y. Shi, B. Su, *Interdiscip. Mater.* **2024**, 3, 133-149.

[63] Y. Xu, S. Zhang, S. Li, Z. Wu, Y. Li, Z. Li, X. Chen, C. Shi, P. Chen, P. Zhang, M. D.

Dickey, B. Su, *npj Flex. Electron.* **2024**, 8, 2.